

Statistical assessment metrics for InSAR atmospheric correction: Applications to generic atmospheric correction online service for InSAR (GACOS) in Eastern China



Ruya Xiao^{a,b,*}, Chen Yu^{b,*}, Zhenhong Li^{c,b}, Xiufeng He^a

^a School of Earth Science and Engineering, Hohai University, Nanjing 211100, China

^b COMET, School of Engineering, Newcastle University, Newcastle upon Tyne NE1 7RU, UK

^c College of Geological Engineering and Geomatics, Chang'an University, Xi'an 710054, China

ARTICLE INFO

Keywords:

InSAR
Atmospheric correction
Performance assessment
Statistical metrics
GACOS
Eastern China

ABSTRACT

The atmospheric effect represents one of the major error sources in Interferometric Synthetic Aperture Radar (InSAR), and its mitigation is found crucial for high-precision InSAR applications. Numerous studies on InSAR atmospheric correction methods and applications covering a wide range of regions worldwide have been reported with varying degrees of success. However, more efforts on the performance assessment are needed, and the conclusions may lack statistical significance due to the limited interferograms involved in most of these analyses. To optimally utilise different InSAR atmospheric correction methods and avoid potential uncertainty caused, appropriate statistical metrics to assess the correction performance must be set up. In this work, we provide a general guideline for statistical assessment of InSAR atmospheric correction. Based on the physical properties of the atmosphere, three metrics are applied: (i) the phase standard deviation which assesses the overall performance of the correction; (ii) the spatial structure function which evaluates the reduction of the long-wavelength atmospheric effect; and (iii) the phase-elevation correlation coefficient which measures the reduction of the stratified component of the atmospheric delay. The performance of the Generic Atmospheric Correction Online Service for InSAR (GACOS) products for two typical terrains in Eastern China is evaluated. Statistical results of the 1250 Sentinel-1 interferograms covering the Yellow River Delta and Shandong hilly region show that (i) GACOS reduces the interferometric phase standard deviation in 84.6% of the interferograms by an average of 36.4%; (ii) the phase decorrelation distance decreases from 321 km to 225 km on average after correction; and (iii) the mean phase-elevation correlation declines by 33.3% for the areas with considerable topographic variations. The results verify the effectiveness of GACOS products in Eastern China for the first time, and the three proposed metrics further characterise the sources of improvement after correction.

1. Introduction

The successful operation of the European Space Agency's (ESA) Sentinel-1 satellites provides unprecedented possibilities and convenience for measuring land surface deformation, escalating InSAR from local, regional practices to large, nationwide applications (e.g., Constantini et al., 2017; Cuenca et al., 2013; Ferretti et al., 2019; Haghghi and Motagh, 2017; Novellino et al., 2017). However, despite its success in measuring large, apparent geophysical signals such as land subsidence, earthquake ruptures, volcanic eruptions and landslides (e.g., Cigna et al., 2013, 2012; Hu et al., 2019; Li et al., 2020a; Wang et al., 2018), InSAR is still limited by its inherent noise sources. One of the

most important of such noise sources is the atmospheric artifact, which is caused by the spatiotemporal variations in the atmospheric refractivity while SAR signals travelling through the atmosphere and makes it difficult to retrieve small magnitude and/or time-varying signals over great distances.

In the past two decades, many efforts have been made to understand the characteristics of the atmosphere, and considerable progress has been made to mitigate the atmospheric effect on InSAR measurements (e.g., Bekaert et al., 2015b; Ding et al., 2008; Foster et al., 2006; Jolivet et al., 2011; Li et al., 2005; Yu et al., 2018b). These methods differ by data availability, correction effectiveness and operational convenience, and most of them have been validated on a case by case basis. Such

* Corresponding author.

E-mail addresses: ruya.xiao@hhu.edu.cn (R. Xiao), chen.yu@newcastle.ac.uk (C. Yu).

validations employed several metrics such as the root-mean-square (RMS) or standard deviation (StdDev) of the interferometric phase (Puysségur et al., 2007; Remy et al., 2003) to evaluate the performance of the atmospheric correction, with limited attention paid to their applicability and limitations. For instance, certain atmospheric effects, such as distance-dependency and elevation-dependency, may not be reflected by the RMS/StdDev. Others have also tried to assess the accuracy and performance of atmospheric delay corrections by ‘ground truth’, such as the Global Positioning System (GPS) estimated Zenith Tropospheric Delay (ZTD) (e.g., Li et al., 2009), but the data availability is an unavoidable problem in practical applications (e.g., lack of GPS stations). In many cases, the atmospheric corrections are simply performed even without verifying or evaluating their accuracies. Furthermore, most of the previous studies only used a limited number of interferograms in their analyses, and the small sample size may lead to conclusions lack of statistical significance.

In order to optimally utilise InSAR atmospheric correction methods and to avoid potential uncertainty caused, it is urgent to develop a generic assessment method without the use of ‘ground truth’ to evaluate the atmospheric correction performance, which is addressed in this paper. Murray et al. (2019) presented a review of several existing atmospheric correction techniques and statistical performance metrics. They used the averaged random windows StdDevs at different spatial scales, frequency domain analysis (power vs distance), and semi-variogram at different distances to compare the efficacy of tropospheric correction methods in the central US and Mexico. In this study, however, we highlight the tropospheric elevation-dependency and its spatial decorrelation distance which is responsible for the long wavelength effect on InSAR measurements. We start from the physical properties of the atmosphere and carefully design three complementary metrics, reflecting the overall noise reduction, long-wavelength atmospheric signal reduction and elevation dependent signal reduction, respectively. These were conducted using the Generic Atmospheric Correction Online Service for InSAR (GACOS) products over Eastern China covering the Yellow River Delta and Shandong hilly region.

2. State-of-the-art InSAR atmospheric correction methods

2.1. InSAR atmospheric correction models

InSAR atmospheric effects are caused by the propagation delay when

microwave signals travel through the two-way pass between the satellite SAR sensor and the Earth’s surface (Ferretti et al., 2001; Hanssen et al., 1999; Li et al., 2005; Massonnet et al., 1994; Zebker et al., 1997). Here, we ignore the ionospheric contributions and only focus on tropospheric noises, and do not strictly distinguish the term ‘atmospheric effects’ from ‘tropospheric effects’.

Atmospheric effects greatly limit the accuracy of InSAR measurements. For example, an error of 0.10–0.14 m for land surface deformation monitoring and possibly 80–290 m for topography mapping may be introduced by a 20% relative humidity change (Zebker et al., 1997). This could lead to misunderstanding in the interpretation of the geophysical processes. Numerous means have been developed to reduce the influence of atmospheric effects to improve the InSAR measurement accuracy. We divide the correction methods into two categories depending on the data used: atmospheric correction with and without external data. Table 1 shows the commonly used atmospheric correction methods and their major advantages and disadvantages.

Correction without external data generally refers to the methods in which there are no atmospheric measurements, such as water vapour, pressure, and temperature, involved in the processing. The phase-based correction models are always based on certain assumptions. For example, the assumption on atmospheric phase screen being uncorrelated in time is often used in time series InSAR analysis (Crosetto et al., 2016; Hooper et al., 2012). Due to the complexity of the Earth’s atmospheric variations, these simple assumptions do not often adequately characterise InSAR atmospheric effects. External data mainly includes the ground observations, satellite-based spectrometer observations, and numerical weather models, which could provide a relatively independent description of the atmospheric delay field. However, the acquisition and processing of the auxiliary data, such as GPS observations and the global meteorological model products, further increases the complexity of the InSAR data processing procedure. The development of easy-to-implement GACOS, to some extent, solves the problem.

2.2. Generic atmospheric correction online service for InSAR (GACOS)

GACOS developed at Newcastle University, United Kingdom, is essentially a method based on numerical weather models. The 90 m resolution SRTM DEM (60° S – 60° N) and ASTER GDEM (for high-latitude regions) are involved in the processing of GACOS atmospheric delay products. It also utilises High RESolution 10-day forecast (HRES

Table 1
The commonly used InSAR atmospheric correction methods.

Categories	Correction methods	Data used	Advantage	Disadvantage	Reference
Correction without external data	Stacking	Interferograms only	Independent on external data, straightforward to implement	Non-independent observations, poor model applicability, signals of interest may be incorrectly removed	Williams et al., 1998; Wright et al., 2001; Zebker et al., 1997
	Time series analysis (PSI/ SBAS ¹ ...)	Interferograms only			Berardino et al., 2002; Ferretti et al., 2011, 2001; Hooper, 2008
	Elevation-dependent phase removal	Interferograms and DEM ²			Bekaert et al., 2015a; Cavalié et al., 2007; Remy et al., 2003
Correction with external data	Ground observations	GPS/weather stations	High temporal resolution	Poor spatial resolution	Li et al., 2006a; Onn and Zebker, 2006; Webley et al., 2002; Xu et al., 2011; Yu et al., 2017
	Satellite observations	MODIS/MERIS/ OLCI ³ ...	Global coverage, high spatial resolution	Daytime only and cloud sensitive	Li et al., 2009, 2006b, 2006c; Li et al., 2012
	Numerical weather models	ECMWF Reanalysis/ NCEP NARR ⁴ ...	Good coverage and high availability	Complex data process	Doin et al., 2009; Foster et al., 2006; Jolivet et al., 2011; Parker et al., 2015

¹ PSI: Persistent Scatterers Interferometry; SBAS: Small Baseline Subset InSAR technique.

² DEM: Digital Elevation Model.

³ MODIS: Moderate Resolution Imaging Spectroradiometer on National Aeronautics and Space Administration’s (NASA) Terra and Aqua satellites; MERIS: Medium Resolution Imaging Spectrometer on ESA’s Envisat platform; OLCI: Ocean and Land Colour Instrument on ESA’s Copernicus Sentinel-3 satellites.

⁴ ECMWF Reanalysis: Reanalysis datasets, e.g., ERA-Interim and the updated version ERA5, released by ECMWF; NCEP NARR: North American Regional Reanalysis by National Centers for Environmental Prediction.

datasets with the resolution of up to $0.1^\circ \times 0.1^\circ$ lat/long grid, 137 vertical levels at every 6 h (<https://www.ecmwf.int/en/forecasts/datasets/set-i>), which is the highest-resolution atmospheric model of ECMWF. By implementation of iterative tropospheric decomposition model (Yu et al., 2017), the stratified and turbulent components are separated from tropospheric delays, and high spatial resolution ZTD maps are generated. Yu et al. (2018b) tested the GACOS performance using eight sites all over the world with phase StdDev or ‘ground truth’, suggesting that the displacement RMS against GPS achieved around 10 mm after correction. In addition to the theoretical and technological evolutions, the service mode of GACOS is also a significant innovation: the free online service reduces the barriers to InSAR atmospheric correction. Users only need to submit a request with the location of their study area and the acquisition time of the SAR data, and then the GACOS ZTD products will be ready-to-use in several to tens of minutes. Unlike GPS method that requires ground observations or the meteorological reanalysis datasets (such as ERA-Interim) which usually have months of delay, GACOS has the advantages of global coverage and near real-time availability. Since launched on 6 June 2017, GACOS has released more than 61,000 tasks all over the world. The distribution of user jobs shown in Fig. 1 demonstrates the areas of interest of the InSAR community.

Numerous researchers have applied GACOS and reported their results (e.g., Albino et al., 2020; Araya and Biggs, 2020; Atzori et al., 2019; Khakim et al., 2020; Kwong et al., 2019; Li et al., 2020; Loibl et al., 2019; Milczarek et al., 2019; Savigas et al., 2019; Vaka et al., 2019; Yip et al., 2019). Albino et al. (2019) compared the GACOS correction with the phase-elevation approach in Agung volcano, Bali using data collected between April and November 2017. They found the coefficient of determination increased from 0.07 to 0.7 for the ascending path, and 0.2 to 0.6 for the descending path interferograms, respectively, and concluded that GACOS corrections were more effective. Anantrasirichai et al. (2019) utilised GACOS in the generation of synthetic datasets for deep learning training, thereby solved the problem of insufficient real data samples for the data-driven methods like the convolutional neural network. They also confirmed that GACOS helped improve the volcano deformation detection accuracy without a significant increase in the computational burden. Lloyd et al. (2019) reported that the GACOS correction reduced the standard deviation of the 2006 Machaze earthquake ENVISAT ASAR interferogram from 12.1 cm to 9.6 cm and was the preferred choice for fault parameter inversion. Murray et al. (2019) applied several methods, including GACOS, NARR, MERRA-2, ERA-Interim, GPS, MODIS, and elevation-dependent model, for InSAR tropospheric correction in the Central United States and Mexico. Random windows standard deviations and semi-variograms were used to evaluate their performance, and results showed that GACOS outperformed all the other tested methods in both study areas.

3. Descriptions of the study site and data

The Yellow River Delta, as an essential industrial and energy base in China with an area of more than 11,600 km², is rich in abundant resources such as oil, gas, and brine. Due to the natural process of sediment deposition and increasing human activities (such as overexploitation of underground resources), the mega delta suffers from severe land subsidence induced hazards, such as the threat to coastal stability, and effective sea-level rise (Higgins et al., 2013). We explore the YRD and its surrounding areas with 83 ascending (track 69, January 2016 to March 2019) and 66 descending (track 76, October 2016 to March 2019) SAR images from Sentinel-1A/B satellites. SAR acquisition times are 10:04 UTC for the ascending path and 22:04 UTC for the descending path, respectively. ZTD maps corresponding to the SAR acquisitions are obtained via GACOS (<http://www.gacos.net>). With the restrictions that the temporal baselines are less than 300 days as well as no more than nine interferometric pairs are generated for each date, we obtain 1250 interferograms in total, including 701 ascending and 549 descending pairs. The processing is undertaken with the GAMMA SAR processor and interferometry software (<https://www.gamma-rs.ch/>). Precise orbit data from ESA is involved in reducing the baseline errors, and the latest version of ALOS World 3D – 30 m (AW3D30) DEM is used for the topographic phase removal. The multi-look factors of 40 (range) and 8 (azimuth) are applied, resulting in interferograms with a spatial resolution of about 120 m. All the interferometric phases are unwrapped using the minimum cost flow method (Eineder et al., 1998) with a coherence threshold of 0.4. As shown in Fig. 2, both tracks cover the plain area, and the mountainous regions with an elevation of up to 1,200 m, which represent the two typical terrain types in Eastern China: plains (the North China Plain) and hills (the Shandong Hills). Since the YRD region is next to the ocean, strong water vapour variations are evident in many interferograms (e.g., Fig. 3(a)). This is why the YRD and Shandong hilly region are chosen as the study sites.

4. Statistical assessment metrics and applications to GACOS products

According to the physical properties of the atmosphere, microwave atmospheric delays are generally considered as the sum of the turbulent component and the vertical stratified component (Hanssen, 2001). The turbulent component of atmospheric effects affects both flat and mountainous terrains, and the vertical stratified component, which is highly correlated with topography, only influences the hilly or mountainous terrain. The atmospheric effects on InSAR measurements span a broad spectrum from long-wavelength to short-wavelength. The long-wavelength signal, which represents a ramp on the interferogram, is

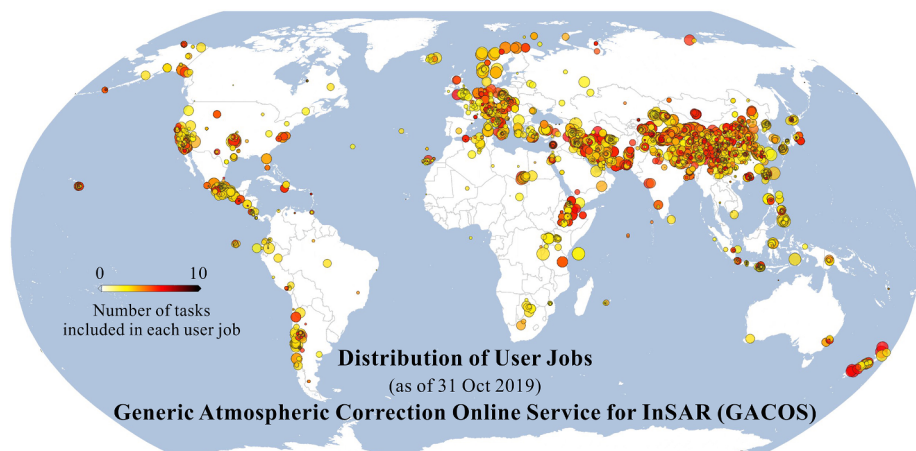


Fig. 1. The distribution of GACOS user jobs from June 2017 to October 2019.

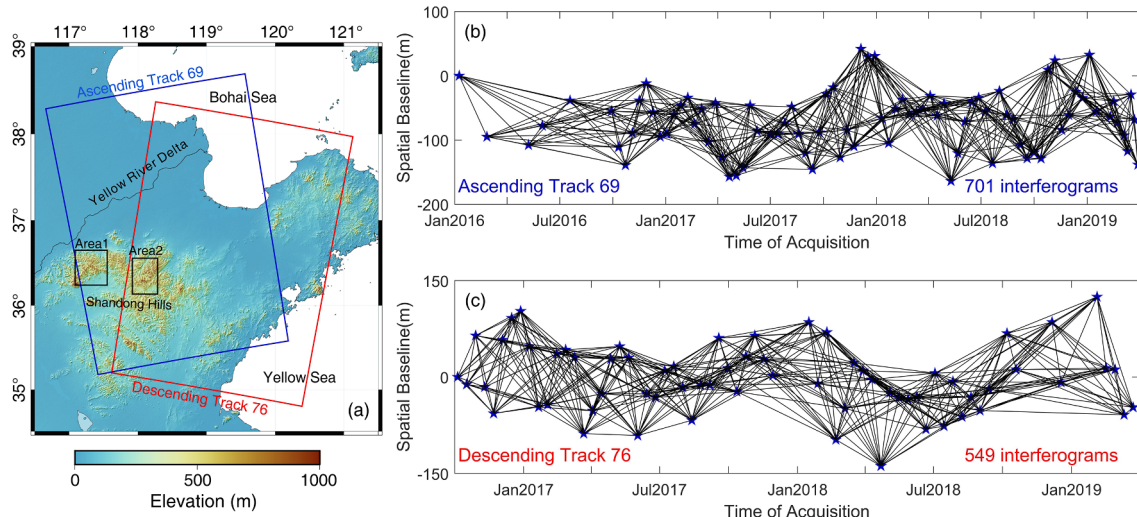


Fig. 2. (a) Overview of the study area covering the YRD and Shandong hilly region with topography as the background map. (b - c) Temporal and spatial baselines of the interferograms.

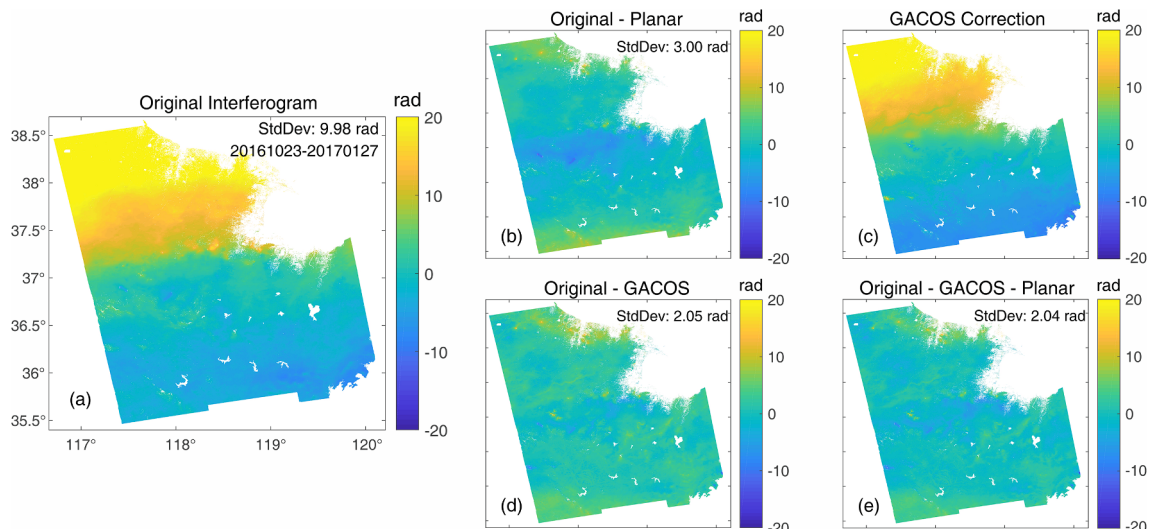


Fig. 3. Example of the interferogram 20161023–20170127 before (a) and after correction (b, d, e). (c) is the GACOS correction.

caused by, for instance, a slow-moving weather system. This is the most dominant error sources in interferograms with a large spatial extent and may indistinguishable from other long-wavelength errors such as the orbital ramps (Shirzaei and Walter, 2011), ocean tide loading (Yu et al., 2020) and solid earth tides (Xu and Sandwell, 2020). The short wavelength signal results from, for example, the combination of the rapidly changing local atmospheric turbulence and the stratified component related to local topography (Yu et al., 2018a). In this section, we first apply the standard deviation of the interferometric phases to assess the overall performance of the correction. Then, the spatial structure function and phase-elevation correlation coefficient are used to evaluate the reductions of the long-wavelength atmospheric signal and the stratified component of the atmospheric effects, respectively. These three indicators are based on the physical properties of the atmosphere and describe their influences on the interferometric phases. This evaluation does not require the ‘ground truth’ and could be considered as a generic assessment method of the InSAR atmospheric correction.

4.1. Rapid assessment of the overall performance

4.1.1. Metric: StdDev of interferogram

The StdDev of the interferometric phase is widely used to assess the quality of the InSAR atmospheric correction under an assumption that there is no surface movement (Doin et al., 2009; Puysségur et al., 2007; Remy et al., 2003). In this situation, the atmospheric delay should be the dominant signal, and the StdDev of the phase observations characterises the significance of atmospheric signals. A decrease in the StdDev demonstrates the reduction of noise level after correction. Fig. 3 is an example showing the interferograms and their standard deviations before and after GACOS correction.

Researchers often use a simple linear or quadratic ramp model to address the long spatial-scale feature in the interferogram (Lohman and Simons, 2005). In the example of Fig. 3, a long-wavelength signal in the original interferogram (Fig. 3(a)) is removed by a planar removal (Fig. 3 (b)) or GACOS correction (Fig. 3(d)), but the details of the results are different. The StdDev of the original interferogram is 9.98 rad, whereas it decreases to 2.05 rad after GACOS correction. The decrease in the StdDev indicates the combined reduction of both the long-wavelength

atmospheric signal and the stratified component of atmospheric effects. The uncertainty falls to 3.00 rad with a phase planar removal from the original phase, at the cost of introducing other errors. It should be emphasised that the negative influence due to the planar removal cannot be thoroughly evaluated only with the single metric. The planar removed result after GACOS correction (Fig. 3(e)) has no significant difference compared with the GACOS correction (Fig. 3(d)). The StdDevs of GACOS-corrected phases without and with a phase planar removal have hardly changed, i.e., 2.05 and 2.04 rad, respectively. This suggests the long-wavelength signal in this interferogram is mainly caused by the atmosphere and successfully mitigated by the GACOS model.

The StdDev is a useful metric for evaluating the noise level of the interferogram but may fail to reflect the spatial structure of the signal. Murray et al. (2019) examined the averaged standard deviations over different spatial scales at random windows, which described the spatial characteristics to some extent. More metrics are needed to describe the spatial features of InSAR atmospheric delays.

4.1.2. Statistical results of StdDev reduction

The StdDev, as well as StdDev reduction for the 1250 interferograms before and after GACOS correction, are shown in Fig. 4. It is observed that the uncertainties of the original interferogram time series seem to have seasonal characteristics. We consider this is due to the four distinct seasons in the study area. Taking the city of Dongying, which is the mouth of the Yellow River, as an example, the monthly average temperature difference in a year can reach 29 °C (-2°C in January and 27 °C in July). More turbulent signals may be expected with higher temperature. Also, the rainfalls in summer (June, July, and August) in the study area accounts for about 65% of the annual precipitation (the temperature and precipitation data come from China Meteorological Data Service Center, <http://data.cma.cn/data/weatherBk.html>). Therefore, a stronger atmospheric signal may exist in the interferometric pairs when SAR images acquired in the summertime are involved.

The StdDev of the interferograms could act as the indication of the uncertainties. In vast majority cases, the uncertainties in the phase observations decrease after GACOS correction. The mean and the standard deviation of the uncertainties for the original interferogram time series are 6.11 and 3.82 rad, respectively, while reducing to 3.85 and 1.95 rad

after correction. The seasonal characteristics in the uncertainties are suppressed after correction, which indicates that GACOS was able to reduce the temporal variability of the interferogram time series.

For the paired StdDevs of interferograms before and after GACOS correction, we use the nonparametric Wilcoxon signed-rank test (Wilcoxon, 1945) to find out if a significant difference exists between the two samples. The null hypothesis stating the two samples have no difference is rejected at the significance level of 0.01, which demonstrates that GACOS takes effect. Since the StdDev decreases after correction in most cases, we can conclude that GACOS performs positively in correcting the atmospheric artifacts.

The absolute changes in the StdDev of the total 1250 interferograms are shown in Fig. 4(b), and the positive values indicate the standard deviations decrease after correction. The maximum, minimum and mean StdDev reductions are 13.22, -6.27 and 1.82 rad, respectively. To better show the improvements after correction, we define the ratio of the StdDev change to the StdDev of the original interferogram, i.e., $\frac{\sigma_o - \sigma_c}{\sigma_o}$, as the atmospheric correction performance, where σ_o is the StdDev of the original interferogram and σ_c is the StdDev of the corrected one. Same as Fig. 4(b), the positive performance means the StdDev decreases after correction. The binned performance is shown in Fig. 5(a) and Fig. 5(b) demonstrates the performance indicator as a function of the original StdDevs.

Fig. 5(a) shows the performance ranged between 20% and 40% accounts for the most proportion, followed by 40–60% and 0–20% intervals, reaching 26.2% and 19.7%, respectively. The StdDevs of 1,057 interferograms fall by 36.4% on average after correction, implying that 84.6% of the interferograms gain positive performance after GACOS correction. Most cases of the negative performance are concentrated in the ‘low signal’ part in Fig. 5(b), which corresponds to a relatively calm atmospheric condition with a StdDev of less than 20 mm (4.53 rad) on a scale of 250 km by 350 km coverage. However, if the original variability is large, like the ‘strong signal’ of more than 30 mm (6.80 rad), GACOS corrections are efficient, and the majority reach performances of greater than 20%.

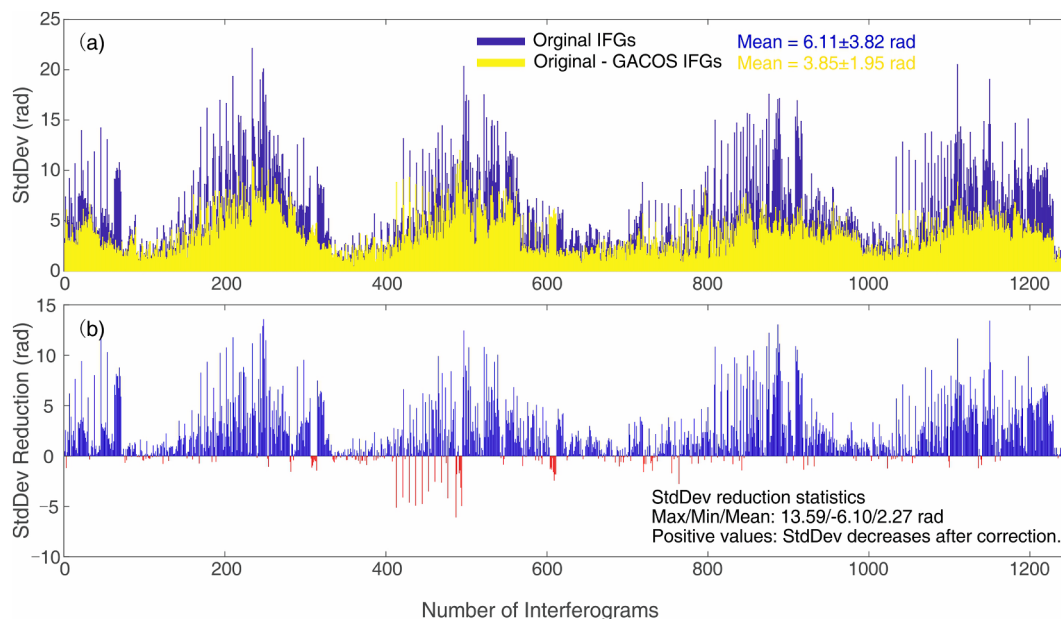


Fig. 4. Standard deviation statistics of the 1250 interferograms. The first 701 interferograms and the latter 549 pairs are from the ascending and descending track, respectively. (a) The StdDevs of the 1250 interferograms before and after correction. (b) The StdDev reductions after GACOS correction. Positive values indicate that the StdDev decreases after correction.

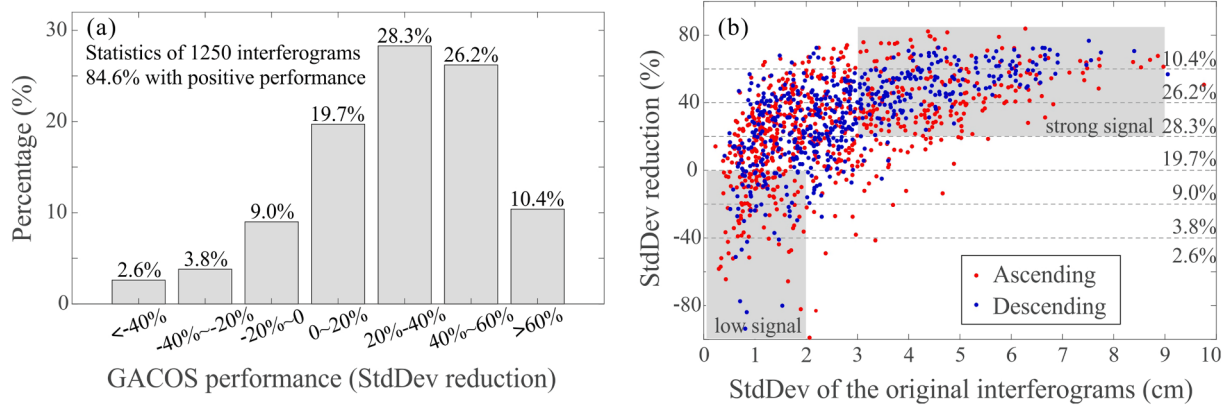


Fig. 5. (a) Histogram of GACOS performance in term of StdDev reduction. (b) Reduction of the StdDev after GACOS correction as a function of the original StdDev.

4.2. Assessment of long-wavelength atmospheric signal reduction

4.2.1. Metric: Spatial structure function

The long-wavelength atmospheric signal, which is distance-dependent, is one of the most common error sources for InSAR observations. To analyse the spatial dependencies, we define the spatial structure function (SSF) as the expected squared difference of a random function $f(x)$ for a covariance stationary (Hanssen, 2001):

$$\gamma(\vec{h}) = E[(f(x) - f(x + \vec{h}))^2] \quad (1)$$

where x is a location and \vec{h} is a vector with the length h . With the homogenous assumption, the directions are ignored and \vec{h} in Equation (1) can be replaced by a scalar h , which only demonstrates the distance (also called lag). In geostatistics, the most commonly used SSF is variogram (or more strictly, semi-variogram) as:

$$\gamma(h) = \frac{1}{2}E[(f(x) - f(x + h))^2] \quad (2)$$

The factor 1/2 in the definition is to get a slightly simpler relation between semi-variogram, γ , and the covariogram, C , as:

$$\gamma(h) = \sigma^2 - C(h) \quad (3)$$

where σ^2 is the variance. Although covariograms are more straightforward to interpret the spatial dependence, semi-variograms are preferable due to their unbiasedness of the estimation. The experimental semi-variogram, which is a visualisation of a possible spatial correlation, is a discrete function calculated by measuring the variability between pairs of points at different distances. Fig. 6 is an example of the semi-variogram and the two-dimensional (2D) SSF results of the original and corrected interferograms.

Fig. 6 shows quantitative comparisons of the SSF results corresponding to the interferograms in Fig. 3. For comparison with the 'semi'-variogram, a factor of 1/2 is applied to the SSF in Equation (1). The experimental semi-variogram results (Fig. 6(a)) demonstrate that the expected squared differences have dramatic decreases after the planar removal or GACOS correction (note the differences in the colour bars). The correction by planar removal looks effective because some 'unwanted' long-wavelength signals are removed. However, it is neither accurate nor sufficient, at the cost of risking to introduce additional uncertainties. The semi-variogram plots of the GACOS-corrected results and the planar removed result after GACOS correction are almost

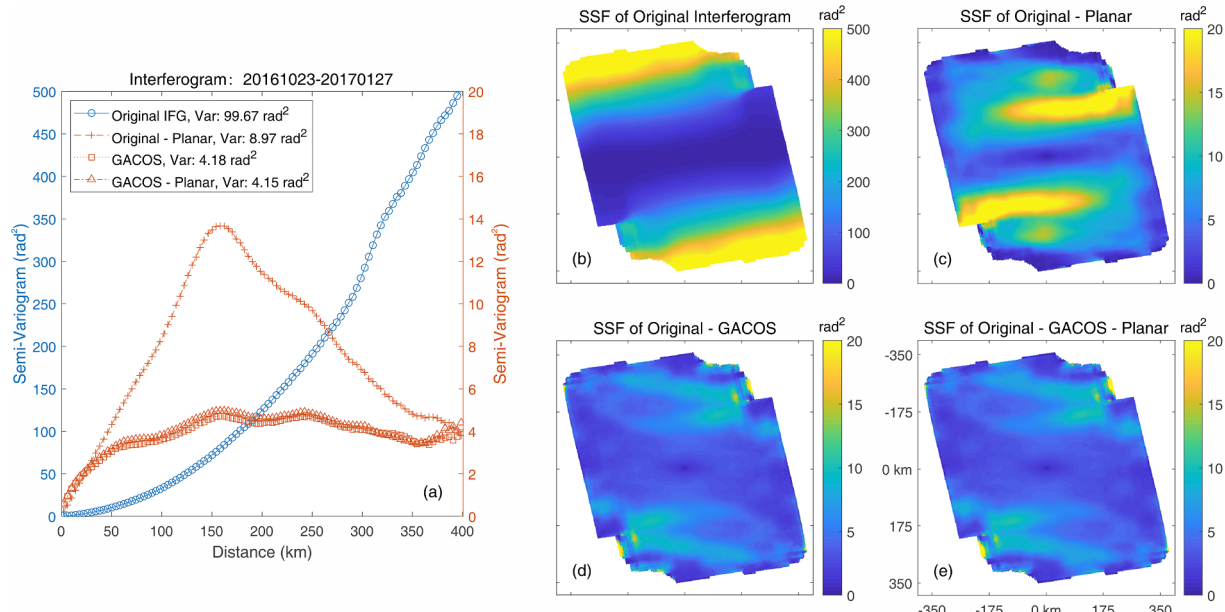


Fig. 6. The SSF results of the interferogram 20161023–20170127. (a) The semi-variogram with the values of the curves corresponding to the vertical axis of the same colour. (b-d) are the 2D SSF of the original interferogram, interferogram corrected with a best-fit planar and interferogram corrected by GACOS, respectively. (e) 2D SSF of the interferogram corrected by a best-fit planar after GACOS correction. Note that the different ranges of vertical axis values in (a) and the colour bars in (b-e).

identical. It is worth mentioning that there are ‘edge effects’ for the rectangular regions and the semi-variogram estimates tend to be less reliable at long distances. That means most of or nearly all the long-wavelength signals, in this case, is caused by atmospheric delay.

The 2D SSF results (Fig. 6 (b - e)) could reveal the directions of the spatial dependencies. The spatially related signals are roughly distributed in a north–south direction in the interferogram. In comparison with the semi-variogram, the SSF results show the spatial heterogeneity of the atmosphere. Although the spatial correlation has a magnitude decrease by the planar removal, it introduces additional errors (Fig. 6(c)). The reason is that the functional models do not well characterise the long-wavelength signals. In the example of Fig. 3, the planar removal is, in fact, unnecessary after GACOS correction.

Except the standard SSF (Hanssen, 2001; Li et al., 2006a), semi-variogram (Murray et al., 2019; Wei et al., 2019), and covariogram (Jonsson, 2002; Lohman and Simons, 2005), several other kinds of SSF, such as the rotational average of the power spectrum (auto-correlation) (Jonsson, 2002; Onn and Zebker, 2006), have also been implemented and discussed in the analyses of atmospheric noise or estimation of covariance functions.

4.2.2. Statistical results of long-wavelength atmospheric signal reduction

In geostatistics, the semi-variogram generally levels out at a certain distance, which is often called as the decorrelation distance. A location separation greater than the decorrelation distance suggests that there is no correlation between the two samples, whereas distance closer than the range are spatially correlated (Smith, 2016). The value that the semi-variogram attains at the decorrelation distance is known as the sill. If a significant trend exists in the data, the semi-variogram may not exhibit a sill. Generally, when a sill is clearly presented in the experimental semi-variogram plot, its value could be used as an estimate of variance (Barnes, 1991). The parameters of the theoretical semi-variogram are determined by fitting based on the experimental semi-variogram. Here, we use the spherical model to estimate the decorrelation distances and sills of the interferograms before and after correction. In the example of Fig. 6(a), the decorrelation distance and sill of the interferogram reduce from 470 km, 197.51 rad² to 114 km, 4.57 rad², respectively. The decorrelation distance and sill statistics of the total 1,250 interferograms are shown in Table 2.

Table 2 shows that the mean decorrelation distance of the interferograms reduces by 96 km to 225 km after GACOS correction. For subsets of ascending and descending tracks, the mean decorrelation distances differ slightly, while the averaged decorrelation distance reductions are close. This exhibits the corrections remove the long-wavelength signals. As the sill is comparable to the variance of the interferogram, the 70.8% reduction of the mean sill depicts a substantial reduction in the noise level. The results suggest GACOS performs better for the descending track interferograms in this case.

The semi-variogram is obtained based on the spatial isotropy assumption, while 2D SSF completely displays the possible anisotropic features of the signals. Because of the spatial information revealed, the SSF is particularly suitable for detecting and quantitatively evaluating the distribution characteristics of the long-wavelength signals in interferograms with wide ranges.

Table 2

The decorrelation distance and sill statistics of the interferograms before and after GACOS correction.

Sample number	Mean decorrelation distance of original interferograms (km)	Mean decorrelation distance of Original - GACOS (km)	Mean sill of original interferograms (rad ²)	Mean sill of Original - GACOS (rad ²)
Ascending	701	316	219	85.40
Descending	549	329	233	87.70
Total	1250	321	225	86.41

4.3. Assessment of vertical stratified delay reduction

4.3.1. Metric: Elevation dependence correlation

The stratified component of the atmospheric effects is caused by the vertical refractivity differences between targets located at different altitudes. The resulting phase difference φ_{mn} between location m and n can be written as:

$$\varphi_{mn} = \int_m^n \Delta N(h) dh \quad (4)$$

where ΔN is the refractivity difference between the two SAR acquisitions, h is the height of the atmospheric layers. Hanssen (2001) reported that the phase differences could reach more than 10 mm for a height difference of 500 m. Jolivet et al. (2014) estimated the correlation coefficient between the interferometric phase and elevation as an alternative to the ratio between turbulent and vertical stratified delays. Here we use the correlation coefficient to describe the elevation dependence in the interferogram. The smaller difference from zero indicates the lower proportion of signals related to the terrain in the interferometric phases. If the absolute value of the correlation decreases after atmospheric correction, it represents mitigation of the vertical stratified components.

Fig. 7 shows an example of the analysis of the stratified delay correction in the Shandong hilly region (Area1 in Fig. 2). For the original interferogram, the correlation between the phase and elevation is 0.81, while it decreases to 0.13 after GACOS correction. The planar function fails to predict the phase-elevation relationship, and atmospheric signals due to elevation dependence as well as a bias exist in the planar removal result. This demonstrates that the function model removal is ineffective or even harmful to the stratified tropospheric delay correction.

From the same interferogram, we select another area (Area2 in Fig. 2) of the mountainous region and show the phase-elevation analysis results as Fig. 8(b - d). The correlation is 0.77 for the original phases and decreases to 0.18 after correction. Compare Fig. 8(d) with Fig. 7(a), we can see that the phase-elevation relationships vary in different areas of the same interferogram.

Fig. 8 displays the interferograms and corrected results of the same area (Area2) on both ascending (Fig. 8(b - d)) and descending (Fig. 8(e - g)) tracks obtained by approximate time. The time difference between the ascending and descending tracks is six days; therefore, the deformation and seasonal decorrelation characteristics variations of the region could be neglected. The difference in results shows that the phase-elevation relationships change with atmospheric conditions even for the same area.

Some phase-estimated correction techniques, such as using a linear relationship between phase and elevation (Cavalié et al., 2007) or a spatially variable power-law correction (Bekaert et al., 2015a), are attempted to mitigate the stratified component of atmospheric effects. In some cases, reasonable results have been achieved. However, since the phase-elevation relationship varies across interferogram and changes with time, the method is empirical. Moreover, in some situations, the deformation correlates with topography (such as the volcano movement), empirical models are highly likely to affect the true signals (Ebmeier et al., 2013).

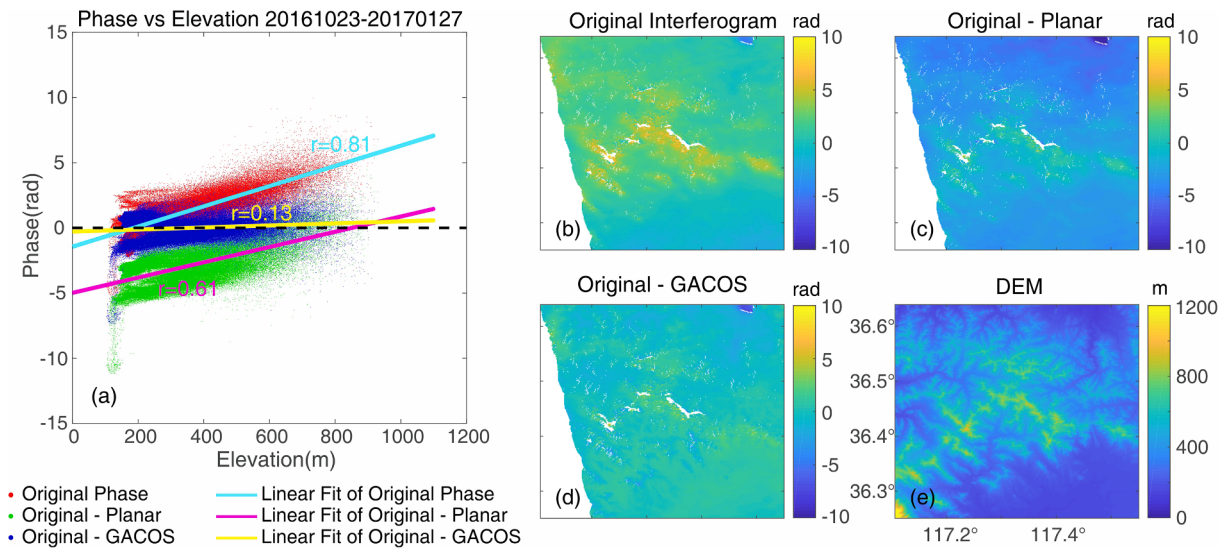


Fig. 7. Phase-elevation analysis of the mountainous terrain Area1 (shown in Fig. 2) in the interferogram 20161023–20170127. (a) Correlations between phase and elevation; (b - d) are the original interferogram, interferogram corrected with a best-fit planar and interferogram corrected by GACOS, respectively; (e) DEM.

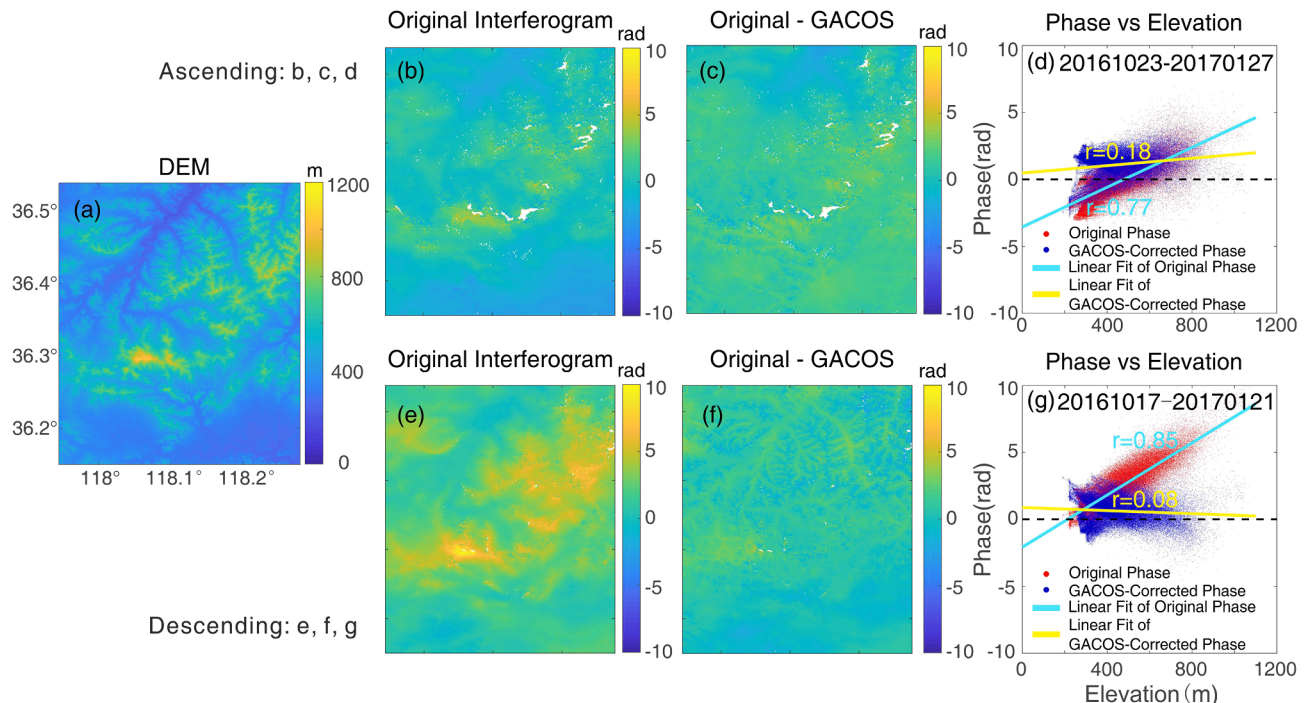


Fig. 8. Phase-elevation analysis of the mountainous terrain Area2 (shown in Fig. 2). (a) DEM; (b - d) are the original, GACOS-corrected interferograms and the phase-elevation correlation, respectively, for the ascending interferogram 20161023–20170127; (e - g) are the original, GACOS-corrected interferograms and the phase-elevation correlation, respectively, for the descending interferogram 20161017–20170121.

4.3.2. Statistical results of vertical stratified delay reduction

The actual relationship between the atmospheric phase and elevation is complicated, or even impossible to model (Parker et al., 2015). Moreover, as the Pearson correlation coefficient is a measurement of a linear relationship, so the absolute value of the correlation coefficient we use here is only an approximate expression of the strength of the relationship between the interferometric phase and topography. Since the vertical stratified component of atmospheric effects only affects the mountainous terrain, in this case, the stratified delay reduction statistics are counted over the region of Shandong hills. The correlations between phase and elevation, before and after GACOS correction, are examined over a range of spatial scales. For each window size, from 10 km to 100

km with a step of 5 km, we take the average of the correlations of randomly selected 1,000 windows across the hilly area in the interferograms. We only examined interferograms that have a correlation of above 0.4, implying a considerable correlation between the original interferometric phase and elevation. Fig. 9 shows examples of the phase-elevation correlation for a single interferogram (Fig. 9a – 9c), and the averages of all interferograms (Fig. 9d).

From Fig. 9, we can see the reduction in the topography-correlated signal after GACOS correction varies in different interferograms. The mean correlation between the phase and elevation over the mountainous areas at different spatial scales, in this case, is 0.54, which reduces to 0.36 after correction. The mean correlation reduction is 0.18,

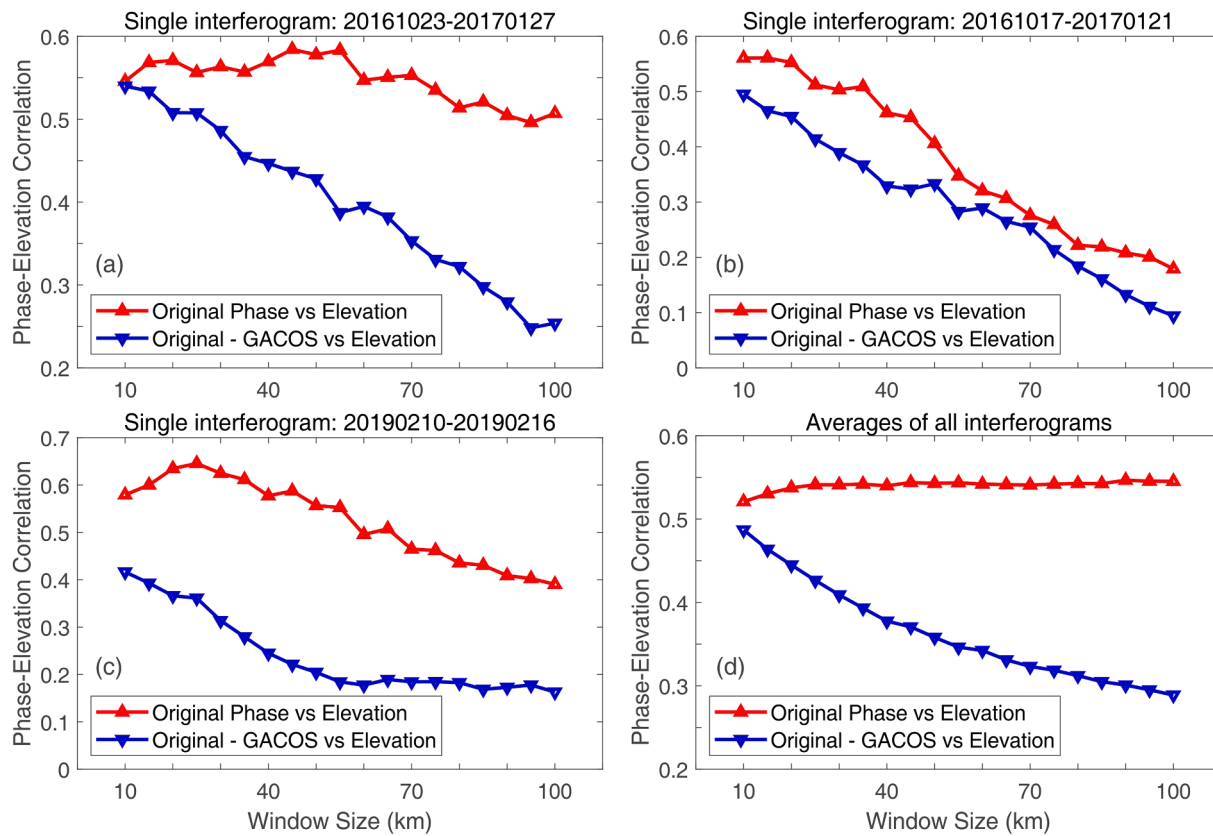


Fig. 9. (a - c) Phase-elevation correlation as a function of distance for example interferograms before and after GACOS correction. (d) The averaged correlations of all interferograms.

suggesting a 33.3% reduction in the topography-correlated signal.

Theoretically, it is feasible to use external vertical profile observations to correct the stratified delay. Due to the unpredictable behaviour of the water vapour in the atmosphere, adequate corrections rely on reliable vertical profile measurements. In practice, the local signal is difficult to be captured and described by the measurements of wider spacing and longer temporal interval. GACOS with the currently highest resolution weather model data is a trade-off or maybe our best shot to

reduce the stratified delay errors.

5. Discussion

Among the three abovementioned metrics, the StdDev could be used for a rapid overall assessment of the atmospheric correction performance. The spatial structure function, including the semi-variogram, can be used to evaluate the reduction of the long-wavelength

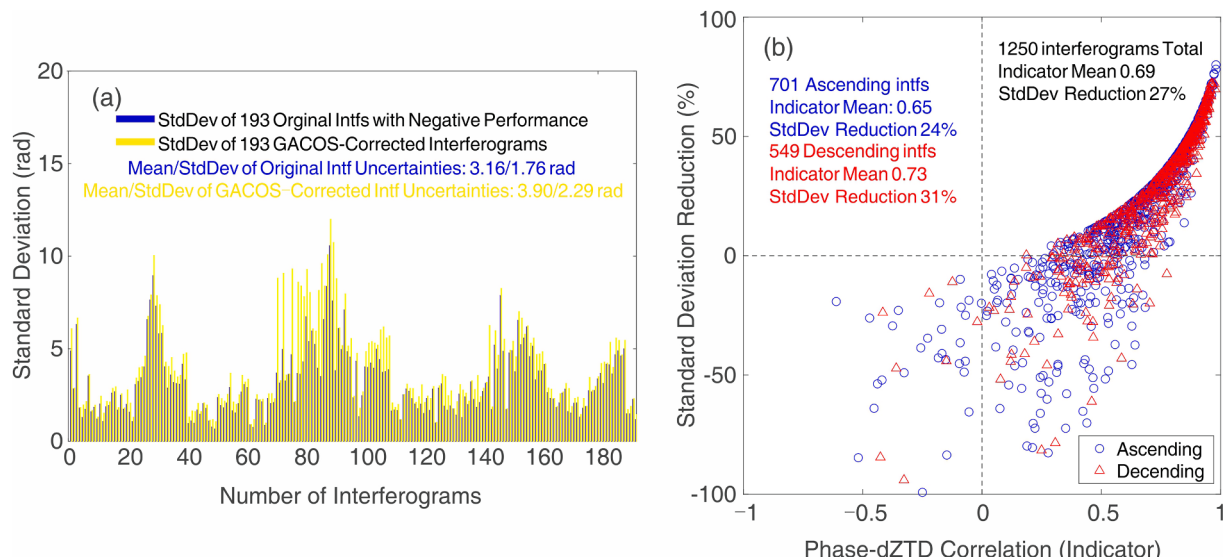


Fig. 10. (a) StdDevs before and after GACOS correction of the 193 interferograms in the negative performance group. (b) Relationship between the phase-dZTD correlation (Indicator) and GACOS performance in terms of the StdDev reduction.

atmospheric signal. The phase-elevation correlation coefficient reflects the relationship between the interferometric phase and the topographic relief, and a decrease indicates a reduction of the stratified atmospheric error. The three complementary metrics provide informative assessment and are essential when integrating atmospheric correction into routine InSAR data processing.

As stated in Fig. 5, 84.6% of the 1250 interferograms gain positive performance after GACOS correction. Here we separately investigate the ‘negative’ performance group, with the StdDevs of the 193 interferograms shown in Fig. 10(a). The mean and standard deviation of the interferogram uncertainties in the negative performance group after correction have slight increases from 3.16, 1.76 rad to 3.90, 2.29 rad, respectively. Table 3 summarises the statistical results of the 193 interferograms before and after correction. It is noted that the increase in the StdDev after correction in the negative performance group is negligible. The mean StdDev rise is only 0.74 rad, i.e., about 3 mm. 81.9% of the interferograms have a StdDev increase of less than 1.13 rad (5 mm), and 92.3% are less than 2.27 rad (10 mm). There are 184 interferograms (95.3%) of which the increases of the StdDev are less than 3.40 rad (15 mm). If the StdDev increase of less than 5 mm is regarded as a positive performance, the total success rate of atmospheric noise correction could reach 97.2% by GACOS.

The mean GACOS performance of the negative performance group is -24.2% . Since the performance is designed as the ratio with the original StdDev as its denominator, when the original variability is small, a tiny StdDev change after correction may result in a high value of the performance. Table 3 shows that 79.8% of the original interferograms in the negative group have the StdDevs of less than 20 mm (‘low signal’ as shown in Fig. 5(b)), corresponding to calm atmospheric conditions. For interferograms with ‘strong signals’, GACOS correction would rarely cause negative performance. It suggests that the performance of GACOS correction is sensitive to the magnitude of the atmospheric signal.

Yu et al. (2018b) proposed the correlation between the phases and the estimated atmospheric delays as an indicator for the applicability of GACOS. Fig. 10(b) represents the correlation coefficient between the interferometric phase and differential ZTD (dZTD) as a function of GACOS performance. For the sake of the aesthetics, seven outliers with performances less than -100% are omitted. The mean of the correlations for the population is 0.69, and the StdDev reduces by 27% on average. For the ascending and descending subsets, they are 0.65, 24% and 0.73, 31%, respectively. Note that with the phase-dZTD correlation increases, GACOS performs better in reducing the atmospheric errors. A higher phase-dZTD correlation suggests that GACOS dZTDs could better describe the atmospheric delay features in the interferograms.

GACOS’s success should attribute to two factors: (i) the high-quality ECMWF HRES product, and (ii) the innovative interpolation algorithm, i.e., the iterative tropospheric decomposition model first developed and used for the generation of high-resolution regional tropospheric PWV fields (Yu et al., 2017) and then applied for InSAR atmospheric correction (Yu et al., 2018a, 2018b). Results showed that the spatial interpolation method based on the iterative tropospheric decomposition model outperformed the Kriging-based methods (Yu et al., 2017). The uncertainties in the correction maps provided by GACOS are mainly from

(i) errors from ECMWF HRES meteorological data, (ii) the spatial resolution difference, and (iii) the time difference between the meteorological data and SAR acquisitions. A new generation of GACOS is under development to further improve the performance, such as integrating the newly released hourly ERA-5 global reanalysis (Hersbach et al., 2019) and 5-minute GPS ZTD estimates.

6. Conclusions

The atmospheric effect is currently one of the most dominant error sources in InSAR datasets and limits the degree of confidence in the interpretation of geophysical processes. Although many methods or products have been proposed and applied to InSAR atmospheric correction, there are few reports on how to evaluate the correction performance systematically. In this paper, we present a guideline for a statistical assessment of InSAR atmospheric correction. Three metrics are implemented to 1250 interferograms covering two typical terrains in Eastern China to evaluate the GACOS atmospheric correction performance with statistical significance:

- The standard deviations of the phase measurements represent the overall noise level of the whole interferogram and the interferogram time series.
- The spatial structure function conveys the scale and distance-dependent information of the atmospheric effects and is particularly applicable to assess the long-wavelength atmospheric signal reduction.
- The phase-elevation correlation assesses the stratified atmospheric delay reduction, which is especially useful in mountainous areas. The relationship between the stratified atmospheric signal and elevation not only varies across the interferogram but also changes with time.

The statistical assessment of GACOS correction for the 1250 interferograms covering the YRD and Shandong hilly region show that (i) GACOS reduces the interferometric phase standard deviation in 84.6% of the cases by an average of 36.4%; (ii) the decorrelation distance decreases from 321 km to 225 km on average after correction; and (iii) the mean phase-elevation correlation declines by 33.3% for the areas with considerable topography variations. The long-wavelength atmospheric signal due to the substantial water vapour variation at the sea-land junction of the YRD, and the stratified component of atmospheric effects in the Shandong hilly region, are suppressed effectively by GACOS, which is vital to InSAR monitoring of the land subsidence and related hazards. It also reflects the applicability of GACOS in Eastern China for the first time. The uncertainty in GACOS products depends on the numerical weather model accuracy as well as the spatial resolution difference and time interval between HRES data and SAR acquisition.

The three proposed metrics are complementary and informative. Statistically significant quantitative assessment of atmospheric correction could allow the users to understand the impact of atmospheric effects and correctly interpret the signals in the interferograms. With the fast-increasing volume of satellite images and the development of automated processing regimes, atmospheric correction and the assessment metrics should be employed routinely in the processing chain. In the new generation of InSAR product services, such as the LiCSAR products (Morishita et al., 2020) of Centre for the Observation and Modelling of Earthquakes, Volcanoes and Tectonics (COMET) and the standard displacement product of NASA’s Advanced Rapid Imaging and Analysis Project (<https://aria.jpl.nasa.gov/>), atmospheric correction acts as an important module or a product layer. It is critical that the users should understand the performance of these atmospheric corrections when applied.

CRediT authorship contribution statement

Ruya Xiao: Conceptualization, Methodology, Validation, Formal

Table 3

Statistical results of the negative performance group (193 interferograms) before and after GACOS correction.

	Percentage among the 193 interferograms			Statistics		
Original StdDev (rad)	<2.27 (10 mm)	<3.40 (15 mm)	<4.53 (20 mm)	MIN	MAX	MEAN
	38.9%	62.7%	79.8%	0.67	10.56	3.16
StdDev Change (rad)	<1.13 (5 mm)	<2.27 (10 mm)	<3.40 (15 mm)	MIN	MAX	MEAN
	81.9%	92.3%	95.3%	-6.10	0.00	-0.74

analysis, Writing - original draft. **Chen Yu:** Conceptualization, Software, Validation, Formal analysis, Investigation, Writing - review & editing. **Zhenhong Li:** Conceptualization, Resources, Writing - review & editing, Supervision, Funding acquisition. **Xiufeng He:** Resources, Writing - review & editing, Supervision.

Declaration of Competing Interest

The authors declared that there is no conflict of interest.

Acknowledgements

This research was supported by National Key R&D Program of China (grant No. 2018YFC0407900); Natural Science Foundation of China (grant Nos. 41804005, 41941019); the Fundamental Research Funds for the Central Universities (grant Nos. 2019B17414, B210202111); the Natural Science Foundation of Jiangsu Province, China (grant No. BK20170869); the Key Laboratory of Land Satellite Remote Sensing Application Center, Ministry of Natural Resources of China (grant No. KLSMTA-202009); and the Chinese Scholarship Council (grant No. 201806715019). Part of this work was also supported by the UK NERC through the Centre for the Observation and Modelling of Earthquakes, Volcanoes and Tectonics (COMET, ref. come30001), and the LICS project (ref. NE/K010794/1). The authors would like to express thanks to the European Space Agency for providing the Copernicus Sentinel-1 SAR data, and the JAXA for the ALOS Global Digital Surface Model ‘ALOS World 3D - 30 m (AW3D30)’ data.

References

- Albino, F., Biggs, J., Syahbana, D.K., 2019. Dyke intrusion between neighbouring arc volcanoes responsible for 2017 pre-eruptive seismic swarm at Agung. *Nat. Commun.* 10, 748. <https://doi.org/10.1038/s41467-019-10854-9>.
- Albino, F., Biggs, J., Yu, C., Li, Z., 2020. Automated Methods for Detecting Volcanic Deformation Using Sentinel-1 InSAR Time Series Illustrated by the 2017–2018 Unrest at Agung, Indonesia. *J. Geophys. Res. Solid Earth* 125. <https://doi.org/10.1029/2019JB017908> e2019JB017908.
- Anantrasirichai, N., Biggs, J., Albino, F., Bull, D., 2019. A deep learning approach to detecting volcano deformation from satellite imagery using synthetic datasets. *Remote Sens. Environ.* 230, 111179. <https://doi.org/10.1016/j.rse.2019.04.032>.
- Araya, M.C., Biggs, J., 2020. Deformation associated with silver transport in Costa Rica: seismic and geodetic observations of the July 2016 Bijagua earthquake sequence. *Geophys. J. Int.* 220, 585–597. <https://doi.org/10.1093/gji/ggz474>.
- Atzori, S., Antonioli, A., Tolomei, C., De Novellis, V., De Luca, C., Monterroso, F., 2019. InSAR full-resolution analysis of the 2017–2018 M>6 earthquakes in Mexico. *Remote Sens. Environ.* 234, 111461. <https://doi.org/10.1016/j.rse.2019.111461>.
- Barnes, R.J., 1991. The variogram sill and the sample variance. *Math. Geol.* 23, 673–678. <https://doi.org/10.1007/BF02065813>.
- Bekaert, D., Hooper, A., Wright, T.J., 2015a. A spatially variable power law tropospheric correction technique for InSAR data. *J. Geophys. Res. Solid Earth* 1–12. <https://doi.org/10.1002/2014JB011557.A>.
- Bekaert, D., Walters, R.J., Wright, T.J., Hooper, A.J., Parker, D.J., 2015b. Statistical comparison of InSAR tropospheric correction techniques. *Remote Sens. Environ.* 170, 40–47. <https://doi.org/10.1016/j.rse.2015.08.035>.
- Berardino, P., Fornaro, G., Lanari, R., Sansosti, E., 2002. A new algorithm for surface deformation monitoring based on small baseline differential SAR interferograms. *IEEE Trans. Geosci. Remote Sens.* 40, 2375–2383. <https://doi.org/10.1109/TGRS.2002.803792>.
- Cavalie, O., Doin, M.P., Lasserre, C., Briole, P., 2007. Ground motion measurement in the Lake Mead area, Nevada, by differential synthetic aperture radar interferometry time series analysis: Probing the lithosphere rheological structure. *J. Geophys. Res. Solid Earth* 112, 1–18. <https://doi.org/10.1029/2006JB004344>.
- Cigna, F., Bianchini, S., Casagli, N., 2013. How to assess landslides activity and intensity with Persistent Scatterer Interferometry (PSI): The PSI-based matrix approach. *Landslides* 10, 267–283. <https://doi.org/10.1007/s10346-012-0335-7>.
- Cigna, F., Osmanoğlu, B., Cabral-Cano, E., Dixon, T.H., Ávila-Olivera, J.A., Garduño-Monroy, V.H., DeMets, C., Wdowinski, S., 2012. Monitoring land subsidence and its induced geological hazard with Synthetic Aperture Radar Interferometry: A case study in Morelia, Mexico. *Remote Sens. Environ.* 117, 146–161. <https://doi.org/10.1016/j.rse.2011.09.005>.
- Costantini, M., Ferretti, A., Minati, F., Falco, S., Trillo, F., Colombo, D., Novali, F., Malvarrosa, F., Mammi, C., Vecchioli, F., Rucci, A., Fumagalli, A., Allievi, J., Ciminelli, M.G., Costabile, S., 2017. Analysis of surface deformations over the whole Italian territory by interferometric processing of ERS, Envisat and COSMO-SkyMed radar data. *Remote Sens. Environ.* 202, 250–275. <https://doi.org/10.1016/j.rse.2017.07.017>.
- Crosetto, M., Monserrat, O., Cuevas-González, M., Devanthéry, N., Crippa, B., 2016. Persistent Scatterer Interferometry: A review. *ISPRS J. Photogramm. Remote Sens.* Doi: 10.1016/j.isprsjprs.2015.10.011.
- Cuenca, M.C., Hanssen, R.F., Hooper, A.J., Arıkan, M., Caro Cuenca, M., Hanssen, R.F., Hooper, A.J., Arıkan, M., 2013. Surface deformation of the whole Netherlands after PSI analysis. *FRINGE Work. Proc.* 1–27.
- Ding, X., Li, Z., Zhu, J., Feng, G., Long, J., 2008. Atmospheric effects on InSAR measurements and their mitigation. *Sensors* 8, 5426–5448. <https://doi.org/10.3390/s8095426>.
- Doin, M.P., Lasserre, C., Peltzer, G., Cavalie, O., Doubre, C., 2009. Corrections of stratified tropospheric delays in SAR interferometry: Validation with global atmospheric models. *J. Appl. Geophys.* 69, 35–50. <https://doi.org/10.1016/j.jappgeo.2009.03.010>.
- Ebmeier, S.K., Biggs, J., Mather, T.A., Amelung, F., 2013. On the lack of InSAR observations of magmatic deformation at Central American volcanoes. *J. Geophys. Res. Solid Earth* 118, 2571–2585. <https://doi.org/10.1002/jgrb.50195>.
- Eineder, M., Hubig, M., Milcke, B., 1998. Unwrapping large interferograms using the minimum cost flow algorithm, in: International Geoscience and Remote Sensing Symposium (IGARSS). IEEE 83–87. <https://doi.org/10.1109/igarss.1998.702806>.
- Ferretti, A., Fumagalli, A., Novali, F., Prati, C., Rocca, F., Rucci, A., 2011. A new algorithm for processing interferometric data-stacks: SqueeSAR. *IEEE Trans. Geosci. Remote Sens.* 49, 3460–3470. <https://doi.org/10.1109/TGRS.2011.2124465>.
- Ferretti, A., Novali, F., Giannico, C., Uttoni, A., Iannicella, I., Mizuno, T., 2019. A SqueeSAR database over the entire Japanese territory. In: 2019 IEEE International Geoscience and Remote Sensing Symposium - IGARSS. Yokohama, Japan, pp. 2078–2080.
- Ferretti, A., Prati, C., Rocca, F., 2001. Permanent scatterers in SAR interferometry. *IEEE Trans. Geosci. Remote Sens.* 39, 8–20. <https://doi.org/10.1109/36.889661>.
- Foster, J., Brooks, B., Cherubini, T., Shacat, C., Businger, S., Werner, C.L., 2006. Mitigating atmospheric noise for InSAR using a high resolution weather model. *Geophys. Res. Lett.* 33. <https://doi.org/10.1029/2006GL026781>.
- Haghghi, M.H., Motagh, M., 2017. Sentinel-1 InSAR over Germany: Large-scale interferometry, atmospheric effects, and ground deformation mapping. *ZFV - Zeitschrift für Geodäsie. Geoinf. Landmanagement* 142, 245–256. <https://doi.org/10.1290/zfv-0174-2017>.
- Hanssen, R.F., 2001. *Radar Interferometry: Data Interpretation and Error Analysis*. Springer Springer Science & Business Media.
- Hanssen, R.F., Weckwerth, T.M., Zebker, H.A., Klees, R., 1999. High-resolution water vapor mapping from interferometric radar measurements. *Science* 283 (80), 1297–1299. <https://doi.org/10.1126/science.283.5406.1297>.
- Hersbach, H., Bell, B., Berrisford, P., Horányi, A., Sabater, J.M., Nicolas, J., Radu, R., Schepers, D., Simmons, A., Soci, C., Dee, D., 2019. Global reanalysis: goodbye ERA-Interim, hello ERA5. *ECMWF Newslet.* 17–24. <https://doi.org/10.2195/vf291hehd7>.
- Higgins, S., Overeem, I., Tanaka, A., Svytski, J.P.M., 2013. Land subsidence at aquaculture facilities in the Yellow River delta, China. *Geophys. Res. Lett.* 40, 3898–3902. <https://doi.org/10.1002/grl.50758>.
- Hooper, A., Bekaert, D., Spaans, K., Arıkan, M., 2012. Recent advances in SAR interferometry time series analysis for measuring crustal deformation. *Tectonophysics* 514–517, 1–13. <https://doi.org/10.1016/j.tecto.2011.10.013>.
- Hooper, A.J., 2008. A multi-temporal InSAR method incorporating both persistent scatterer and small baseline approaches. *Geophys. Res. Lett.* 35. <https://doi.org/10.1029/2008GL034654>.
- Hu, L., Dai, K., Xing, C., Li, Z., Tomás, R., Clark, B., Shi, X., Chen, M., Zhang, R., Qiu, Q., Lu, Y., 2019. Land subsidence in Beijing and its relationship with geological faults revealed by Sentinel-1 InSAR observations. *Int. J. Appl. Earth Obs. Geoinf.* 82, 101886. <https://doi.org/10.1016/j.jag.2019.05.019>.
- Jolivet, R., Agram, P.S., Lin, N.Y., Simons, M., Doin, M.P., Peltzer, G., Li, Z., 2014. Improving InSAR geodesy using Global Atmospheric Models. *J. Geophys. Res. Solid Earth* 119, 2324–2341. <https://doi.org/10.1002/2013JB010588.Received>.
- Jolivet, R., Grandin, R., Lasserre, C., Doin, M.P., Peltzer, G., 2011. Systematic InSAR tropospheric phase delay corrections from global meteorological reanalysis data. *Geophys. Res. Lett.* 38, 6. <https://doi.org/10.1029/2011GL048757>.
- Jonsson, S., 2002. *Modeling Volcano and earthquake deformation from satellite radar interferometric observations*. Stanford University, Stanford Dep. Geophys.
- Khakim, M.Y.N., Bama, A.A., Yustian, I., Poerwono, P., Tsuji, T., Matsuoka, T., 2020. Peatland subsidence and vegetation cover degradation as impacts of the 2015 El Niño event revealed by Sentinel-1A SAR data. *Int. J. Appl. Earth Obs. Geoinf.* 84, 101953. <https://doi.org/10.1016/j.jag.2019.101953>.
- Kwong, K.B., DeShon, H.R., Kim, J.W., Lu, Z., 2019. Resolving Teleseismic Earthquake Catalog and InSAR Data Discrepancies in Absolute Space to Explore Rupture Complexity Along the Ecuadorian Megathrust Fault. *J. Geophys. Res. Solid Earth* 124, 6703–6719. <https://doi.org/10.1029/2018JB016271>.
- Li, Y., Jiao, Q., Hu, X., Li, Z., Li, B., Zhang, J., Jiang, W., Luo, Y., Li, Q., Ba, R., 2020a. Detecting the slope movement after the 2018 Baige Landslides based on ground-based and space-borne radar observations. *Int. J. Appl. Earth Obs. Geoinf.* 84, 101949. <https://doi.org/10.1016/j.jag.2019.101949>.
- Li, Y., Tian, Y., Yu, C., Su, Z., Jiang, W., Li, Z., Zhang, J., Luo, Y., Li, B., 2020b. Present-day interseismic deformation characteristics of the Beng Co-Dongqiao conjugate fault system in central Tibet: implications from InSAR observations. *Geophys. J. Int.* 221, 492–503. <https://doi.org/10.1093/gji/ggaa014>.
- Li, Z., Fielding, E.J., Cross, P., Muller, J.P., 2006a. Interferometric synthetic aperture radar atmospheric correction: GPS topography-dependent turbulence model. *J. Geophys. Res. Solid Earth* 111. <https://doi.org/10.1029/2005JB003711>.
- Li, Z., Fielding, E.J., Cross, P., Muller, J.P., 2006b. Interferometric synthetic aperture radar atmospheric correction: Medium Resolution Imaging Spectrometer and

- Advanced Synthetic Aperture Radar integration. *Geophys. Res. Lett.* 33 <https://doi.org/10.1029/2005GL025299>.
- Li, Z., Fielding, E.J., Cross, P., Preusker, R., 2009. Advanced InSAR atmospheric correction: MERIS/MODIS combination and stacked water vapour models. *Int. J. Remote Sens.* 30, 3343–3363. <https://doi.org/10.1080/01431160802562172>.
- Li, Z., Muller, J.P., Cross, P., Albert, P., Fischer, J., Bennartz, R., 2006c. Assessment of the potential of MERIS near-infrared water vapour products to correct ASAR interferometric measurements. *Int. J. Remote Sens.* 27, 349–365. <https://doi.org/10.1080/01431160500307342>.
- Li, Z., Muller, J.P., Cross, P., Fielding, E.J., 2005. Interferometric synthetic aperture radar (InSAR) atmospheric correction: GPS, Moderate Resolution Imaging Spectroradiometer (MODIS), and InSAR integration. *J. Geophys. Res. Solid Earth* 110, 1–10. <https://doi.org/10.1029/2004JB003446>.
- Li, Z., Xu, W., Feng, G., Hu, J., Wang, C., Ding, X., Zhu, J., 2012. Correcting atmospheric effects on InSAR with MERIS water vapour data and elevation-dependent interpolation model. *Geophys. J. Int.* 189, 898–910. <https://doi.org/10.1111/j.1365-246X.2012.05432.x>.
- Lloyd, R., Biggs, J., Copley, A., 2019. The decade-long Machaze-Zinave aftershock sequence in the slowly straining Mozambique Rift. *Geophys. J. Int.* 217, 504–531. <https://doi.org/10.1093/gji/ggz033>.
- Lohman, R.B., Simons, M., 2005. Some thoughts on the use of InSAR data to constrain models of surface deformation: Noise structure and data downampling. *Geochemistry, Geophys., Geosystems* 6. <https://doi.org/10.1029/2004GC000841>.
- Loibl, D., Bookhagen, B., Valade, S., Schneider, C., 2019. OSARIS, the "Open Source SAR Investigation System" for Automated Parallel InSAR Processing of Sentinel-1 Time Series Data With Special Emphasis on Cryosphere Applications. *Front. Earth Sci.* 7 <https://doi.org/10.3389/feart.2019.00172>.
- Massonnet, D., Feigl, K., Rossi, M., Adragna, F., 1994. Radar interferometric mapping of deformation in the year after the Landers earthquake. *Nature* 369, 227–230. <https://doi.org/10.1038/369227a0>.
- Milczarek, W., Kopeć, A., Gąbićki, D., 2019. Estimation of Tropospheric and Ionospheric Delay in DInSAR Calculations: Case Study of Areas Showing (Natural and Induced) Seismic Activity. *Remote Sens.* 11, 621. <https://doi.org/10.3390/rs11060621>.
- Morishita, Y., Lazecky, M., Wright, T.J., Weiss, J.R., Elliott, J.R., Hooper, A., 2020. LiCSBAS: An open-source insar time series analysis package integrated with the LiCSAP automated sentinel-1 InSAR processor. *Remote Sens.* 12, 424. <https://doi.org/10.3390/rs12030424>.
- Murray, K.D., Bekaert, D.P.S., Lohman, R.B., 2019. Tropospheric corrections for InSAR: Statistical assessments and applications to the Central United States and Mexico. *Remote Sens. Environ.* 232, 111326. <https://doi.org/10.1016/j.rse.2019.111326>.
- Novellino, A., Cigna, F., Brahma, M., Sowter, A., Bateson, L., Marsh, S., 2017. Assessing the feasibility of a national InSAR ground deformation map of great britain with sentinel-1. *Geosci.* 7, 19. <https://doi.org/10.3390/geosciences7020019>.
- Onn, F., Zebker, H.A., 2006. Correction for interferometric synthetic aperture radar atmospheric phase artifacts using time series of zenith wet delay observations from a GPS network. *J. Geophys. Res. Solid Earth* 111. <https://doi.org/10.1029/2005JB004012>.
- Parker, A.L., Biggs, J., Walters, R.J., Ebmeier, S.K., Wright, T.J., Teanby, N.A., Lu, Z., 2015. Systematic assessment of atmospheric uncertainties for InSAR data at volcanic arcs using large-scale atmospheric models: Application to the Cascade volcanoes. *United States. Remote Sens. Environ.* 170, 102–114. <https://doi.org/10.1016/j.rse.2015.09.003>.
- Puységur, B., Michel, R., Avouac, J.P., 2007. Tropospheric phase delay in interferometric synthetic aperture radar estimated from meteorological model and multispectral imagery. *J. Geophys. Res. Solid Earth* 112. <https://doi.org/10.1029/2006JB004352>.
- Remy, D., Bonvalot, S., Briole, P., Murakami, M., 2003. Accurate measurements of tropospheric effects in volcanic areas from SAR interferometry data: Application to Sakurajima volcano (Japan). *Earth Planet. Sci. Lett.* 213, 299–310. [https://doi.org/10.1016/S0012-821X\(03\)00331-5](https://doi.org/10.1016/S0012-821X(03)00331-5).
- Shirzaei, M., Walter, T.R., 2011. Estimating the effect of satellite orbital error using wavelet-based robust regression applied to InSAR deformation data. *IEEE Trans. Geosci. Remote Sens.* 49, 4600–4605. <https://doi.org/10.1109/TGRS.2011.2143419>.
- Smith, T.E., 2016. Notebook on Spatial Data Analysis [WWW Document]. <https://doi.org/10.3389/fninf.2010.00009>.
- Svigkas, N., Atzori, S., Kiratzi, A., Tolomei, C., Salvi, S., 2019. Isolation of swarm sources using InSAR: The case of the February 2017 seismic swarm in western Anatolia (Turkey). *Geophys. J. Int.* 217, 1479–1495. <https://doi.org/10.1093/gji/gzz093>.
- Vaka, D.S., Rao, Y.S., Bhattacharya, A., 2019. Surface displacements of the 12 November 2017 Iran-Iraq earthquake derived using SAR interferometry. *Geocarto Int.* <https://doi.org/10.1080/10106049.2019.1618927>.
- Wang, T., DeGrandpre, K., Lu, Z., Freymueller, J.T., 2018. Complex surface deformation of Akutan volcano, Alaska revealed from InSAR time series. *Int. J. Appl. Earth Obs. Geoinf.* 64, 171–180. <https://doi.org/10.1016/j.jag.2017.09.001>.
- Webley, P.W., Bingley, R.M., Dodson, A.H., Wadge, G., Waugh, S.J., James, I.N., 2002. Atmospheric water vapour correction to InSAR surface motion measurements on mountains: Results from a dense GPS network on Mount Etna. *Phys. Chem. Earth* 27, 363–370. [https://doi.org/10.1016/S1474-7065\(02\)00013-X](https://doi.org/10.1016/S1474-7065(02)00013-X).
- Wei, J., Li, Z., Hu, J., Feng, G., Duan, M., 2019. Anisotropy of atmospheric delay in InSAR and its effect on InSAR atmospheric correction. *J. Geod.* 93, 241–265. <https://doi.org/10.1007/s00190-018-1155-x>.
- Wilcoxon, F., 1945. Individual Comparisons by Ranking Methods. *Biometrics Bull.* 1, 80–83.
- Williams, S., Bock, Y., Fang, P., 1998. Integrated satellite interferometry: Tropospheric noise, GPS estimates and implications for interferometric synthetic aperture radar products. *J. Geophys. Res. Solid Earth* 103, 27051–27067. <https://doi.org/10.1029/98jb02794>.
- Wright, T., Parsons, B., Fielding, E., 2001. Measurement of interseismic strain accumulation across the North Anatolian Fault by satellite radar interferometry. *Geophys. Res. Lett.* 28, 2117–2120. <https://doi.org/10.1029/2000GL012850>.
- Xu, W., Li, Z., Ding, X., Zhu, J., 2011. Interpolating atmospheric water vapor delay by incorporating terrain elevation information. *J. Geod.* 85, 555–564. <https://doi.org/10.1007/s00190-011-0456-0>.
- Xu, X., Sandwell, D.T., 2020. Toward Absolute Phase Change Recovery with InSAR: Correcting for Earth Tides and Phase Unwrapping Ambiguities. *IEEE Trans. Geosci. Remote Sens.* 58, 726–733. <https://doi.org/10.1109/TGRS.2019.2940207>.
- Yip, S.T.H., Biggs, J., Albino, F., 2019. Reevaluating Volcanic Deformation Using Atmospheric Corrections: Implications for the Magmatic System of Agung Volcano. *Indonesia. Geophys. Res. Lett.* 46, 13704–13711. <https://doi.org/10.1029/2019GL085233>.
- Yu, C., Li, Z., Penna, N.T., 2018a. Interferometric synthetic aperture radar atmospheric correction using a GPS-based iterative tropospheric decomposition model. *Remote Sens. Environ.* 204, 109–121. <https://doi.org/10.1016/j.rse.2017.10.038>.
- Yu, C., Li, Z., Penna, N.T., Crippa, P., 2018b. Generic Atmospheric Correction Model for Interferometric Synthetic Aperture Radar Observations. *J. Geophys. Res. Solid Earth* 123, 9202–9222. <https://doi.org/10.1029/2017JB015305>.
- Yu, C., Penna, N., Li, Z., 2020. Ocean Tide Loading Effects on InSAR Observations Over Wide Regions. *Geophys. Res. Lett.* 47 <https://doi.org/10.1029/2020GL088184>.
- Yu, C., Penna, N.T., Li, Z., 2017. Generation of real-time mode high-resolution water vapor fields from GPS observations. *J. Geophys. Res.* 122, 2008–2025. <https://doi.org/10.1002/2016JD025753>.
- Zebker, H.A., Rosen, P.A., Hensley, S., 1997. Atmospheric effects in interferometric synthetic aperture radar surface deformation and topographic maps. *J. Geophys. Res. Solid Earth* 102, 7547–7563. <https://doi.org/10.1029/96jb03804>.